PHYSICAL REVIEW D **105,** 084012 (2022)

Double null evolution of a scalar field in Kerr spacetime

Marcos A. Argañaraz[1] and Osvaldo M. Moreschi[2]

[1]*Facultad de Matemática Astronomía, Física y Computación (FaMAF),*
Universidad Nacional de Córdoba, X5000HUA Córdoba, Argentina
[2]*Instituto de Física Enrique Gaviola (IFEG), CONICET, Ciudad Universitaria,*
X5000HUA Córdoba, Argentina

(Received 15 December 2021; accepted 14 March 2022; published 11 April 2022)

We have developed and implemented a numerical scheme and code that computes the evolution of the massless scalar field wave equation in Kerr spacetime, using double null coordinates. The results show a smooth behavior across the event horizon, making it possible to give initial data outside the event horizon, evolve the scalar field across the horizon, and keep the evolution even inside the black hole. This is the first time that a double null evolution is performed for a scalar field in Kerr spacetime.

DOI: 10.1103/PhysRevD.105.084012

I. INTRODUCTION

The scalar field equation in Kerr spacetime is a very useful subject of study because it helps to understand the behavior of the spacetime under linear perturbations, since it shares the principal part of the wave equation for any other spin weighted quantity. This was shown in Ref. [1], where gravitational and electromagnetic perturbations of Kerr spacetime were characterized by a master equation with the same principal part as that of the massless scalar wave equation.

Recent observational evidence, namely, the first gravitational wave detection of black hole collisions [2] and the first black hole image [3], use Kerr spacetime as the main candidate for the final state of a real black hole. Since empirical evidence only comes from black holes with angular momentum, the theoretical interest on studding perturbations of Kerr spacetime has renewed motivation.

In order to cover exterior and interior black hole regions, many analytical and numerical works have used coordinates that are not null to avoid coordinate singularities, such as, for example, [4–10]. In all these works, there is a clear need of interpreting results at the interior. In this region a direct causal interpretation given by a double null coordinate system would be ideal. However, such coordinate system was not available at the time of all cited works.

In this work we tackle the evolution of a massless scalar field in Kerr spacetime, from the black hole exterior to the interior (crossing the event horizon) and using characteristic data on a pair of null coordinates. The use of a formalism that uses characteristic data and evolves over retarded times is known in the studies of the asymptotic structure of asymptotically flat spacetimes [11,12], in which one usually deals with initial data on a section of future null infinity and evolves in the three-dimensional null conformal infinity. Here we present a new approach to the numerical study of a massless scalar field in Kerr spacetime, based on a double characteristic initial value problem in contrast to previous analytical and numerical calculations that have concentrated on the Cauchy initial value problem (see, for example, [13]). Thus, in our new framework one can evolve in one or the other of the null coordinates, using characteristic initial data on two null hypersurfaces.

One of the advantages of using characteristic initial data is the absence of constraints. Moreover, the use of null coordinates allows for direct causal interpretation of results and easy compactification of spacetime regions.

From a general perspective, there are important analytical results that show the feasibility of the characteristic initial value problem in general relativity [14,15]. In Ref. [14], it is shown that the Hilbert-Einstein equations are well posed when data are given on two transversely intersecting null hypersurfaces.

The state of the art on the double null scalar field evolution can be traced to the linearized regime in the case of Schwarzschild spacetime [16] and recently to the nonlinear regime for spherically symmetric spacetimes [17], which due to its symmetries reduces to a two-dimensional problem. In Kerr spacetime, the situation is much more difficult and even initial data without angular dependence will produce at least a three-dimensional problem.

In this article we prove that it is feasible to use our double null coordinate system [18] to evolve a characteristic initial value problem across the horizon of a black hole with angular momentum, from analytical and numerical points of view. This coordinate system has the advantage of being smooth in a global sense, since it covers the spacetime with full angular dependence and it is adapted to the horizons without any divergences. We emphasize this because previous attempts in the literature [19–22] have different types of divergent behavior at the axis of symmetry, as we have shown in [18]. In contrast, in this article we show analytically and numerically that our coordinate system does not present any computational hazard and that one can integrate a double null hyperbolic problem in Kerr spacetime for the desired lapse of null time, retarded or advanced. This is the first time that a double null evolution of a scalar field is performed in Kerr spacetime.

The article is organized as follows: In Sec. II we resume and introduce the definition of center-of-mass (c.m.) double null coordinates [18] that we use. In Sec. III we start with the scalar field equation in Boyer-Lindquist coordinates [23], and then we express it in c.m. double null coordinates. We show from an analytic perspective that the equation is well behaved across future and past exterior horizons; consequently, the scalar field evolution can cross the horizon in a regular way. In Sec. IV we present a second-order-accurate numerical scheme that is adapted for double null coordinates simulations. In Sec. V we present the numerical results, together with two independent precision tests: one of them about the precision order of the numerical scheme and the other one related to energy conservation. The results of these tests indicate that the scalar field behavior revealed in our numerical solutions is highly reliable and with the desired accuracy. In Sec. VI, we summarize the main aspects of our contribution.

II. DOUBLE NULL COORDINATES

In this section we will briefly introduce the definition of c.m. double null coordinates for Kerr spacetime. For a detailed and complete description, see [18].

To make our notation explicit, let us begin by writing the Kerr line element using Boyer-Lindquist [23] coordinates

$$\begin{aligned} ds^2 = {} & \left(1-\frac{2mr}{\Sigma}\right)dt^2 + \frac{4amr}{\Sigma}\sin^2(\theta)dtd\phi \\ & -\frac{\Sigma}{\Delta}dr^2 - \Sigma d\theta^2 - \frac{\Upsilon}{\Sigma}\sin^2(\theta)d\phi^2, \end{aligned} \tag{1}$$

with

$$\begin{aligned} &\Sigma = r^2 + a^2\cos^2(\theta), \qquad \Delta = r^2 + a^2 - 2mr, \\ &\Upsilon = (r^2+a^2)^2 - \Delta a^2 \sin^2(\theta) \geqq 0, \end{aligned} \tag{2}$$

where the parameter m denotes the mass, and the angular momentum of the black holes is given by $J = am$.

Since the principal null congruences have twist, they do not help in the search for natural null hypersurfaces. Therefore, one has to start by considering all possible null geodesics. From the work of [24,25], the most general null geodesic congruence for the Kerr spacetime can be expressed in terms of its tangent vector

$$V^a = \dot{t}\left(\frac{\partial}{\partial t}\right)^a + \dot{r}\left(\frac{\partial}{\partial r}\right)^a + \dot{\theta}\left(\frac{\partial}{\partial \theta}\right)^a + \dot{\phi}\left(\frac{\partial}{\partial \phi}\right)^a. \tag{3}$$

All the steps of our definition are shorter and simpler if we work with the one form V_a, which in Boyer-Lindquist coordinates is

$$\begin{aligned} V_a &= g_{ab}V^b \\ &= Edt_a - \dot{r}\frac{\Sigma}{\Delta}dr_a - \dot{\theta}\Sigma d\theta_a - L_z d\phi_a \\ &= Edt_a - \frac{\pm_{oi}\sqrt{[(r^2+a^2)E - aL_z]^2 - K\Delta}}{\Delta}dr_a \\ &\quad - \left(\pm\sqrt{K - [Ea\sin(\theta) - \frac{L_z}{\sin(\theta)}]^2}\right)d\theta_a - L_z d\phi_a, \end{aligned} \tag{4}$$

where E, L_z, and K (Carter constant) are conserved quantities along each geodesic. The sign $\pm_{oi}$ determines the congruence character. We call ℓ_a (with $\pm_{oi} = +$) the outgoing most general null congruence and $\mathfrak{n}_a$ (with $\pm_{oi} = -$) the ingoing one.

Making an adequate choice of null geodesics (see [18]), where $E = 1$, $L_z = 0$, and $K = K(r,\theta)$, one obtains a pair of null congruences that allows one to define outgoing u and ingoing v null coordinates

$$\begin{aligned} \ell_a &= (du)_a \\ &= dt_a - \frac{\sqrt{(r^2+a^2)^2 - K(r,\theta)\Delta}}{\Delta}dr_a \\ &\quad - \pm|_h \sqrt{K(r,\theta) - a^2\sin(\theta)^2}d\theta_a, \end{aligned} \tag{5}$$

$$\begin{aligned} \mathfrak{n}_a &= (dv)_a \\ &= dt_a + \frac{\sqrt{(r^2+a^2)^2 - K(r,\theta)\Delta}}{\Delta}dr_a \\ &\quad \pm|_h \sqrt{K(r,\theta) - a^2\sin(\theta)^2}d\theta_a, \end{aligned} \tag{6}$$

where the function $K(r,\theta)$ must satisfy

$$\sqrt{(r^2+a^2)^2 - K\Delta}\frac{\partial K}{\partial r} \pm|_h \sqrt{K - (a\sin(\theta))^2}\frac{\partial K}{\partial \theta} = 0. \tag{7}$$

The expression $\pm|_h$ determines the sign for $\dot{\theta}$, which is chosen from thinking of the behavior of spheroidal coordinates, close to a sphere, in the limit as one approaches future null infinity following an outgoing null geodesic, so that we take (+) for the northern hemisphere and (−) for the southern hemisphere. It can be seen then that by imposing Eq. (7) one guarantees that K is constant along each null geodesic of the congruence.

The structure of Eq. (7) suggests to work with the auxiliary function k defined from

$$K(r,\theta) = a^2 \sin(\theta)^2 + k^2(r,\theta), \tag{8}$$

so that the function $K(r,\theta)$ can be expressed in terms of $k(r,\theta)$. All the details about the numerical scheme that we use and its solutions can be found in [18].

In order to obtain a null coordinate system that is well behaved across the horizon, one also has to define a new angular coordinate

$$d\varphi_{\pm_{oi}} = d\phi - \pm_{oi} \frac{a}{\Delta} dr. \tag{9}$$

Then in the outer region, we can define the extended version of those null coordinates as

$$U = -\exp(-\kappa_+ u) \tag{10}$$

and

$$V = \exp(\kappa_+ v). \tag{11}$$

In the inner region $U > 0$, one would use the relation

$$U = \exp(\kappa_+ u_{\mathrm{inner}}), \tag{12}$$

where u_{inner} is the analogous inner version of the null coordinate u in the outer region and κ_+ is the surface gravity given by $\kappa_+ = \sqrt{m^2 - a^2}/(2m(m + \sqrt{m^2 - a^2}))$. The complete and detailed description of interior regions in terms of double null coordinates will be published elsewhere.

III. SCALAR FIELD EQUATION

In the work of Teukolsky [1], the master equation for linear perturbations of Kerr spacetime was presented for different type of sources, namely, scalar field (spin $s = 0$), electromagnetic field (spin $s = 1$), and gravitational radiation (spin $s = 2$). In Boyer-Lindquist coordinates [23], the massless scalar field equation ($s = 0$) can be written as

$$\begin{aligned} &\left[\frac{(r^2+a^2)^2}{\Delta} - a^2 \sin(\theta)^2\right] \frac{\partial^2 \Phi}{\partial t^2} + \frac{4amr}{\Delta} \frac{\partial^2 \Phi}{\partial t \partial \phi} \\ &\quad + \left[\frac{a^2}{\Delta} - \frac{1}{\sin(\theta)^2}\right] \frac{\partial^2 \Phi}{\partial \phi^2} - \frac{\partial}{\partial r}\left(\Delta \frac{\partial \Phi}{\partial r}\right) \\ &\quad - \frac{1}{\sin(\theta)} \frac{\partial}{\partial \theta}\left(\sin(\theta) \frac{\partial \Phi}{\partial \theta}\right) = 0. \end{aligned} \tag{13}$$

It must be noted that Eq. (13) is not regular at the horizon $\Delta = 0$. Therefore, the scalar field evolution can not cross the horizon unless a coordinate transformation is made. To sort out this issue, one could use another coordinate system, such as, for example, the Kerr-Schild coordinates or the c.m. double null coordinates [18] that will be used in this work. The main advantage of null coordinates is that they capture the causal character of the whole spacetime. Therefore, a causal interpretation of results follows directly.

A. Scalar field equation in coordinates $\{u, v, \theta, \varphi\}$

The coordinate transformation can be done in two steps. First, we can transform from Boyer-Lindquist coordinates [23] $\{t, r, \theta, \phi\}$ to the c.m. double null coordinates [18] $\{u, v, \tilde{\theta}, \varphi\}$. The relations between both coordinate systems are

$$du = dt - \frac{\sqrt{\mathcal{R}}}{\Delta} dr - k(r,\theta) d\theta, \tag{14}$$

$$dv = dt + \frac{\sqrt{\mathcal{R}}}{\Delta} dr + k(r,\theta) d\theta, \tag{15}$$

$$d\tilde{\theta} = d\theta, \tag{16}$$

and Eq. (9), where

$$\mathcal{R} = (r^2 + a^2)^2 - K\Delta, \tag{17}$$

$$k(r,\theta) = \pm|_h \sqrt{K(r,\theta) - a^2 \sin(\theta)^2}. \tag{18}$$

After a standard transformation procedure, one obtains

$$\begin{aligned} &4\left(\frac{\mathcal{R}}{\Delta} + k(r,\theta)^2\right) \frac{\partial^2 \Phi}{\partial v \partial u} - 2k(r,\theta)\left(\frac{\partial^2 \Phi}{\partial v \partial \theta} - \frac{\partial^2 \Phi}{\partial u \partial \theta}\right) \\ &\quad - \left(\frac{\partial \Phi}{\partial v} - \frac{\partial \Phi}{\partial u}\right)\left(\partial_r \sqrt{\mathcal{R}} + \partial_\theta k(r,\theta) + \frac{\cos(\theta)}{\sin(\theta)} k(r,\theta)\right) \\ &\quad + \frac{2a}{\Delta}(2mr \pm_{io} \sqrt{\mathcal{R}})\left(\frac{\partial^2 \Phi}{\partial v \partial \varphi}\right) \\ &\quad + \frac{2a}{\Delta}(2mr - \pm_{io} \sqrt{\mathcal{R}})\left(\frac{\partial^2 \Phi}{\partial u \partial \varphi}\right) \\ &\quad - \frac{1}{\sin(\theta)^2}\left(\frac{\partial^2 \Phi}{\partial \varphi^2}\right) - \frac{1}{\sin(\theta)} \frac{\partial}{\partial \theta}\left(\sin(\theta) \frac{\partial \Phi}{\partial \theta}\right) = 0. \end{aligned} \tag{19}$$

Note that if we take the limit $a \to 0$ we have that $k(r,\theta) \to 0$, $\Sigma \to r^2$, $\partial_r \sqrt{\mathcal{R}} \to 2r$, and $\frac{\mathcal{R}}{\Delta} \to r^2/(1 - \frac{2m}{r})$. In this limit, Eq. (19) gets reduced to the massless scalar field equation for Schwarzschild spacetime (in Eddington-Finkelstein null coordinates), as one could expect.

B. Scalar field equation in coordinates $\{U, V, \theta, \varphi\}$

The second step is to transform coordinates from $\{u, v, \theta, \varphi\}$ to the extended ones $\{U, V, \theta, \varphi\}$. These new coordinates will allow one to cross the horizon in a regular way. The relevant relations between both coordinate systems are

$$dU = -\kappa U du, \tag{20}$$

$$dV = \kappa V dv; \tag{21}$$

then

$$\frac{\partial}{\partial u} = \frac{\partial U}{\partial u}\frac{\partial}{\partial U} = -\kappa U \frac{\partial}{\partial U}, \tag{22}$$

$$\frac{\partial}{\partial v} = \frac{\partial V}{\partial v}\frac{\partial}{\partial V} = \kappa V \frac{\partial}{\partial V}. \tag{23}$$

Therefore, if one replace Eqs. (22) and (23) in (19), the massless scalar field equation can be expressed as

$$\begin{aligned} &-4\kappa^2 \frac{\Upsilon}{\Delta} UV \frac{\partial^2 \Phi}{\partial V \partial U} - \kappa \left(V \frac{\partial \Phi}{\partial V} + U \frac{\partial \Phi}{\partial U} \right) \left(\partial_r \sqrt{\mathcal{R}} + \partial_\theta k + \frac{\cos(\theta)}{\sin(\theta)} k \right) + \frac{2a\kappa V}{\Delta} (2mr \pm|_{oi} \sqrt{\mathcal{R}}) \left(\frac{\partial^2 \Phi}{\partial V \partial \varphi} \right) \\ &- \frac{2a\kappa U}{\Delta} (2mr - \pm|_{oi} \sqrt{\mathcal{R}}) \left(\frac{\partial^2 \Phi}{\partial U \partial \varphi} \right) - 2\kappa k(r,\theta) \left(V \frac{\partial^2 \Phi}{\partial V \partial \theta} + U \frac{\partial^2 \Phi}{\partial U \partial \theta} \right) \\ &- \frac{1}{\sin(\theta)^2} \left(\frac{\partial^2 \Phi}{\partial \varphi^2} \right) - \frac{1}{\sin(\theta)} \frac{\partial}{\partial \theta} \left(\sin(\theta) \frac{\partial \Phi}{\partial \theta} \right) = 0, \end{aligned} \tag{24}$$

where we have used the relation (see [18])

$$\Upsilon = \mathcal{R} + k(r,\theta)^2 \Delta. \tag{25}$$

Note that, in Eq. (24), the spin coefficient ρ of the related c.m. null tetrad appears as a factor, namely,

$$\left(\partial_r \sqrt{\mathcal{R}} + \partial_\theta k + \frac{\cos(\theta)}{\sin(\theta)} k \right) = -2\Sigma\rho. \tag{26}$$

In our previous work [18], we have shown that ρ is well behaved and easy to compute for all angular domains $\theta \in [0, \pi]$. However, if one uses other previous definitions of null coordinates, that factor will have a divergent behavior at the axis of symmetry. For example in Hayward's null coordinates definition [19], the related spin coefficient ρ_{Hayward} is divergent at the axis of symmetry ($\theta = 0, \pi$).

C. Behavior across horizons

Recalling that $r_\pm = m \pm \sqrt{m^2 - a^2}$ are the roots of Δ, one can see that in Eq. (24) there are three coefficients that seem to have problems at $r = r_+$, $\Delta = 0$, for both exterior horizons H_f (future) and H_p (past). These coefficients are located at the first, third, and fourth term of Eq. (24). It will be shown that all of them are well behaved. Note that, for exterior horizons, one has to choose $\kappa = \kappa_+$.

Let us start with the third and fourth terms of Eq. (24). The strategy is to take a path to approach H_f. One can follow a curve maintaining V constant, $V = V_0$, meanwhile one approaches (r_+). In that case, we have

$$U|_{V=V_0,(r\approx r_+)} \approx -\frac{e^{2\kappa_+ r}(r_-)^{\frac{r_-}{r_+}}}{V_0 r_+ (r - r_-)^{\frac{r_+ + r_-}{r_+}}} \Delta. \tag{27}$$

From [18], we know that the well-behaved angular coordinate at H_f is φ_-, then one must take $(\pm_{io} = -)$. Therefore, the coefficients of the third and fourth terms of Eq. (24) near H_f behave like

$$\frac{2a\kappa_+ V}{\Delta}(2mr - \sqrt{\mathcal{R}}) \approx -2a\kappa_+ V_0, \tag{28}$$

$$\begin{aligned} &\frac{-2a\kappa_+ U}{\Delta}(2mr + \sqrt{\mathcal{R}}) \\ &\quad \approx \frac{2a\kappa_+ e^{2\kappa_+ r}(r_-)^{\frac{r_-}{r_+}}}{V_0 r_+ (r - r_-)^{\frac{r_+ + r_-}{r_+}}} (2mr + r^2 + a^2). \end{aligned} \tag{29}$$

This means that the third and fourth terms of Eq. (24) are well behaved at future exterior horizon H_f.

In an analogous way it can be shown that both terms have a good behavior at past horizon H_p. One can follow a curve maintaining U constant, $U = U_0$, as one approaches (r_+). In that case we have

$$V|_{U=U_0,(r\approx r_-)} \approx -\frac{e^{2\kappa_+ r}(r_-)^{\frac{r_-}{r_+}}}{U_0 r_+ (r - r_-)^{\frac{r_+ + r_-}{r_+}}} \Delta, \tag{30}$$

where the well-behaved angular coordinate at H_p is φ_+; that is, one must take $(\pm_{io} = +)$. Therefore, near H_p the coefficients behave like

$$\begin{aligned} &\frac{2a\kappa V}{\Delta}(2mr + \sqrt{\mathcal{R}}) \\ &\quad \approx -\frac{2a\kappa_+ e^{2\kappa_+ r}(r_-)^{\frac{r_-}{r_+}}}{U_0 r_+ (r - r_-)^{\frac{r_+ + r_-}{r_+}}} (2mr + r^2 + a^2), \end{aligned} \tag{31}$$

$$-\frac{2a\kappa_+ U}{\Delta}(2mr - \sqrt{\mathcal{R}}) \approx 2a\kappa_+ U_0. \tag{32}$$

This means that the third and fourth terms of Eq. (24) are well behaved at past exterior horizon H_p.

The remaining coefficient to analyze appears in the first term of Eq. (24). From [18], we have a useful expression for the product UV which is valid even at $r = r_+$,

$$UV|_{\kappa=\kappa_+} = \frac{-e^{2\kappa_+(r+\int_0^\theta k(r,\theta')d\theta')}(r_-)^{\frac{r_-}{r_+}}}{(r_+)(r-r_-)^{\frac{r_++r_-}{r_+}}}\Delta. \tag{33}$$

Then, near (r_+), for both exterior horizons H_f and H_p, such coefficient can be expressed like

$$4\kappa^2\frac{\Upsilon}{\Delta}UV|_{r=r_+} = \frac{-4\kappa^2\Upsilon e^{2\kappa_+(r_++\int_0^\theta k(r_+,\theta')d\theta')}(r_-)^{\frac{r_-}{r_+}}}{(r_+)(r_+-r_-)^{\frac{r_++r_-}{r_+}}}, \tag{34}$$

which is clearly well behaved.

It is important to mention that the c.m. double null coordinates can also be extended through the Cauchy horizons C^+ and C^-, which are located in the inner region at $r = r_-$. Such study will be published in a future article.

IV. NUMERICAL SCHEME

A. Generic scheme

In this section we will describe a generic numerical scheme that is adapted for double null coordinates simulations. It is based on previous works [16,17], where double null simulations were carried out.

We can start with Eq. (24), leaving in the left-hand side the cross-derivative and putting all the rest of the terms in the right-hand side. Then, we can express it with a more compact notation

$$\frac{\partial^2\Phi}{\partial V\partial U} = F\left(x^\alpha, \Phi, \frac{\partial\Phi}{\partial x^\alpha}, \frac{\partial^2\Phi}{\partial x^\alpha\partial x^\beta}\right). \tag{35}$$

The main idea of the algorithm is to work with a basic grid that consists of four-point grid blocks, see Fig. 1.

Then one can use centered finite-difference approximations

$$\begin{aligned}\frac{\partial^2\Phi}{\partial V\partial U}\approx&\frac{1}{4\delta U\delta V}[\Phi(U+\delta U,V+\delta V)\\&-\Phi(U+\delta U,V-\delta V)-\Phi(U-\delta U,V+\delta V)\\&+\Phi(U-\delta U,V-\delta V)]+\mathcal{O}(\delta U)^2+\mathcal{O}(\delta V)^2.\end{aligned} \tag{36}$$

If one considers

$$\delta U = \frac{h_U}{2}, \tag{37}$$

and then evaluates (36) at point 0 (see Fig. 1), one obtains

$$\left(\frac{\partial^2\Phi}{\partial V\partial U}\right)\Big|_0 \approx \frac{\Phi_4-\Phi_3-\Phi_2+\Phi_1}{h_U h_V}+\mathcal{O}[h_U^2]+\mathcal{O}[h_V^2], \tag{38}$$

which is exactly the same expression used in [16,17]. Following the same notation of Eq. (35),

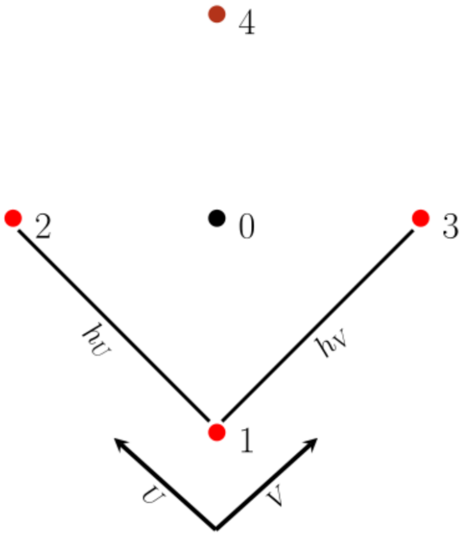

FIG. 1. Basic grid of double null numerical scheme. The scalar field values are known at points 1–3. The value at point 4 needs to be approximated by the numerical scheme.

$$\left(\frac{\partial^2\Phi}{\partial V\partial U}\right)\Big|_0 = F|_0, \tag{39}$$

where

$$F|_0 = F\left(U_0, V_0, \Phi|_0, \frac{\partial\Phi}{\partial x^\alpha}\Big|_0, \frac{\partial^2\Phi}{\partial x^\alpha\partial x^\beta}\Big|_0\right), \tag{40}$$

we can express the numeric approximation of Φ_4 as

$$\begin{aligned}\Phi_4 \approx{}& \Phi_3 + \Phi_2 - \Phi_1 + (h_U h_V)F|_0\\&+\mathcal{O}[h_V h_U^3]+\mathcal{O}[h_U h_V^3].\end{aligned} \tag{41}$$

In the case of equal grid spacing in U and V, namely, $(h_U = h_V = h)$, we get the central equation of the double null numerical scheme

$$\Phi_4 \approx \Phi_3 + \Phi_2 - \Phi_1 + h^2F|_0 + \mathcal{O}[h^4]. \tag{42}$$

The algorithm is as follows: One starts with known data in Φ_1, Φ_2, and Φ_3 and then Φ_4 is estimated by (42). In the next step, one moves to another grid point by an increment h_V along the V direction, and again one has a four-point grid block that allows one to integrate Φ_4. Once $V_{\max}$ is reached, where $V \in [V_{\min}, V_{\max}]$, one returns to $V = V_{\min}$, but now the grid point displacement is along the U direction by an amount of h_U. Then, the whole process is repeated again. This algorithm is consistent with initial data given over a region $\{(U_{\min}, V) \cup (U, V_{\min})\}$.

If the grid U, V has N^2 points, to reach the last grid point $U_{\max}$, $V_{\max}$, one needs to perform N^2 integration steps. Therefore, the global error will be

$$e_{\mathrm{global}} = N^2 e_{\mathrm{local}}. \tag{43}$$

From (42), in this case the local error is

$$e_{\mathrm{local}} \approx \mathcal{O}[h^4]. \tag{44}$$

If the grid spacing is $h = \mathcal{O}[1/N]$, one has

$$e_{\mathrm{global}} \approx \mathcal{O}[h^2]. \tag{45}$$

This means that the double null numerical scheme is second-order accurate.

In practice, $F|_0$ has to be computed numerically, whose value we call $(F|_0)_{\mathrm{num}}$. Then, to satisfy (45) one needs to approximate the right-hand side of (35) with a local error of order $\mathcal{O}(h^2)$, which means that

$$(F|_0)_{\mathrm{num}} \approx (F|_0)_{\mathrm{exact}} + \mathcal{O}(h^2). \tag{46}$$

In this way, the product $h^2 (F|_0)_{\mathrm{num}}$ that appears in Eq. (42), will give the expected local error (44), from which one obtains the desired global error (45).

B. Numerical scheme in Kerr spacetime

Unlike previous works of double null simulations in spherical symmetric spacetimes [16,17], in the Kerr case (with axial symmetry), the partial differential Eq. (35) involves first- and second-order angular derivatives and even cross-derivatives between null and angular coordinates.

To compute such derivatives, one must consider the angular dependence

$$\Phi \equiv \Phi(U, V, \theta, \varphi), \quad \text{with} \quad \theta \in [0, \pi], \varphi \in [0, 2\pi]. \tag{47}$$

Each cross-derivative null angular, is computed as

$$\left(\frac{\partial^2 \Phi}{\partial U \partial \theta}\right)\Bigg|_0 = D^n_\theta\left[\left(\frac{\partial \Phi}{\partial U}\right)\Bigg|_0\right] + \mathcal{O}(h_U)^2 + \mathcal{O}(h_\theta)^n, \tag{48}$$

$$\left(\frac{\partial^2 \Phi}{\partial V \partial \theta}\right)\Bigg|_0 = D^n_\theta\left[\left(\frac{\partial \Phi}{\partial V}\right)\Bigg|_0\right] + \mathcal{O}(h_V)^2 + \mathcal{O}(h_\theta)^n, \tag{49}$$

$$\left(\frac{\partial^2 \Phi}{\partial U \partial \varphi}\right)\Bigg|_0 = D^n_\varphi\left[\left(\frac{\partial \Phi}{\partial U}\right)\Bigg|_0\right] + \mathcal{O}(h_U)^2 + \mathcal{O}(h_\varphi)^n, \tag{50}$$

$$\left(\frac{\partial^2 \Phi}{\partial V \partial \varphi}\right)\Bigg|_0 = D^n_\varphi\left[\left(\frac{\partial \Phi}{\partial U}\right)\Bigg|_0\right] + \mathcal{O}(h_V)^2 + \mathcal{O}(h_\varphi)^n, \tag{51}$$

and the angular derivatives as

$$\left(\frac{\partial^2 \Phi}{\partial \theta^2}\right)\Bigg|_0 = DD^n_\theta[(\Phi)|_0] + \mathcal{O}(h_\theta)^n, \tag{52}$$

$$\left(\frac{\partial^2 \Phi}{\partial \varphi^2}\right)\Bigg|_0 = DD^n_\varphi[(\Phi)|_0] + \mathcal{O}(h_\varphi)^n, \tag{53}$$

$$\left(\frac{\partial \Phi}{\partial \theta}\right)\Bigg|_0 = D^n_\theta[(\Phi)|_0] + \mathcal{O}(h_\theta)^n, \tag{54}$$

where $\Phi|_0$ can be approximated in the same way as [16,17]

$$(\Phi)|_0 = \left(\frac{\Phi_3 + \Phi_2}{2}\right) + \mathcal{O}(h^2). \tag{55}$$

The operators $D^n_{x^a}$ and $DD^n_{x^a}$ are the well-known finite-difference approximations for the first- and second-order derivatives, with error order $\mathcal{O}(h_{x^a})^n$. In this work we use $n = 4$ for angular derivatives. As usual in hyperbolic equations, there will be a grid spacing relation between null coordinates and angular ones, in order to preserve the numerical stability. Such condition is known as the Courant-Friedrichs-Lewy (CFL) condition.

The previous derivative approximations are used to compute the right-hand side of Eq. (35),

$$(F|_0)_{\mathrm{num}} = (F|_0)_{\mathrm{exact}} + \mathcal{O}(h^2) + \mathcal{O}(h_\theta)^4 + \mathcal{O}(h_\varphi)^4. \tag{56}$$

In this way, one obtains the desired precision (46), such that the numerical scheme becomes second-order accurate, with global error (45).

Finally, it is important to mention that, in the same way as [17], we will use a two step predictor-corrector scheme. In the first step, the derivatives with respect to null coordinates are computed with first-order approximations, namely,

$$\left(\frac{\partial \tilde{\Phi}}{\partial U}\right)\Bigg|_0 = \frac{\Phi_3 - \Phi_1}{h_U} + \mathcal{O}(h_U), \tag{57}$$

$$\left(\frac{\partial \tilde{\Phi}}{\partial V}\right)\Bigg|_0 = \frac{\Phi_2 - \Phi_1}{h_V} + \mathcal{O}(h_V), \tag{58}$$

where the angular and cross-derivatives are computed with Eqs. (48)–(54). After this first step, one has

$$(\tilde{F}|_0)_{\mathrm{num}} = (F|_0)_{\mathrm{exact}} + \mathcal{O}(h), \tag{59}$$

$$(\tilde{\Phi}_4)_{\mathrm{num}} = (\Phi_4)_{\mathrm{exact}} + \mathcal{O}(h^3). \tag{60}$$

In the second step, one uses $\tilde{\Phi}_4$ to compute the derivatives as

$$\left(\frac{\partial \Phi}{\partial U}\right)\Bigg|_0 \approx \frac{\Phi_3 - \Phi_1 + \tilde{\Phi}_4 - \Phi_2}{2h_U} + \mathcal{O}(h_U)^2, \tag{61}$$

$$\left(\frac{\partial \Phi}{\partial V}\right)\Bigg|_0 \approx \frac{\Phi_2 - \Phi_1 + \tilde{\Phi}_4 - \Phi_3}{2h_V} + \mathcal{O}(h_V)^2, \tag{62}$$

and then one computes the cross-derivatives (48)–(51) with the desired order for the error. Note that, in this second step, there is no need to compute angular derivatives again, because in the first step they were already computed (52)–(54).

In this way, after the second step, one approximates $F|_0$ with the desired accuracy, namely,

$$(F|_0)_{\mathrm{num}} = (F|_0)_{\mathrm{exact}} + \mathcal{O}(h^2), \tag{63}$$

$$(\Phi_4)_{\mathrm{num}} = (\Phi_4)_{\mathrm{exact}} + \mathcal{O}(h^4). \tag{64}$$

C. Axially symmetric initial data

The numerical difficulties of computing the derivatives with respect to φ coordinate at the poles, which is usual in spherical coordinates, demands of one to work with different coordinate patches for the numeric computation, as was done in [26]. This is a nontrivial task and demands a long time development. Therefore, the compromise between results and time leads us to consider axially symmetric initial data, which allows us to avoid the mentioned difficulties, but also maintains enough complexity to give nontrivial initial data with angular dependence on θ.

If the initial data do not depend on coordinate φ, we can write Eq. (24) as

$$\begin{aligned}\frac{\partial^2\Phi}{\partial V\partial U} = {}& \left[\frac{\Delta}{4\Upsilon\kappa^2 UV}\right] \\ &\times\left\{-\kappa\left(V\frac{\partial\Phi}{\partial V}+U\frac{\partial\Phi}{\partial U}\right)\left(\partial_r\sqrt{\mathcal{R}}+\partial_\theta k+\frac{\cos(\theta)}{\sin(\theta)}k\right)\right. \\ &-2\kappa k\left(V\frac{\partial^2\Phi}{\partial V\partial\theta}+U\frac{\partial^2\Phi}{\partial U\partial\theta}\right) \\ &\left.-\frac{1}{\sin(\theta)}\frac{\partial}{\partial\theta}\left(\sin(\theta)\frac{\partial\Phi}{\partial\theta}\right)\right\}. \end{aligned}\tag{65}$$

Note that the right-hand overall factor in Eq. (65) is well behaved at the exterior horizon, see (34).

D. Angular dependence on θ

The axial symmetry and smoothness of $\Phi(U,V,\theta)$ is related to the fact that the θ first derivative is zero at the poles, namely,

$$\left.\frac{\partial\Phi}{\partial\theta}\right|_{\theta=0,\pi} = 0. \tag{66}$$

Then we can compute the last term of Eq. (65) using l'Hôpital rule

$$\left.\left[\frac{1}{\sin(\theta)}\frac{\partial}{\partial\theta}\left(\sin(\theta)\frac{\partial\Phi}{\partial\theta}\right)\right]\right|_{\theta=0,\pi} = 2\left.\left(\frac{\partial^2\Phi}{\partial\theta^2}\right)\right|_{\theta=0,\pi}. \tag{67}$$

As we have already indicated previously, we can compute fourth-order θ derivatives using centered finite-difference operators. For instance, for the first derivative with respect to θ, one has

$$\begin{aligned}D^4_\theta[\Phi(\theta)] = {}& \frac{1}{12h_\theta}(-\Phi(\theta+2h_\theta)+8\Phi(\theta+h_\theta) \\ &-8\Phi(\theta-h_\theta)+\Phi(\theta-2h_\theta))+\mathcal{O}(h_\theta)^4,\end{aligned}\tag{68}$$

and for the second derivative

$$\begin{aligned}DD^4_\theta[\Phi(\theta)] = {}& \frac{1}{12h_\theta^2}(-\Phi(\theta+2h_\theta)+16\Phi(\theta+h_\theta) \\ &-30\Phi(\theta)+16\Phi(\theta-h_\theta)-\Phi(\theta-2h_\theta)) \\ &+\mathcal{O}(h_\theta)^4.\end{aligned}\tag{69}$$

Then, to use these centered expressions, even at the first two grid points near $\theta = 0$ and the last two grid points near $\theta = \pi$, one can use ghost points

$$\begin{aligned}\Phi_{\mathrm{ghost}}(\theta = 0-h_\theta) &= \Phi(\theta = 0+h_\theta),\\ \Phi_{\mathrm{ghost}}(\theta = 0-2h_\theta) &= \Phi(\theta = 0+2h_\theta),\\ \Phi_{\mathrm{ghost}}(\theta = \pi+h_\theta) &= \Phi(\theta = \pi-h_\theta),\\ \Phi_{\mathrm{ghost}}(\theta = \pi+2h_\theta) &= \Phi(\theta = \pi-2h_\theta),\end{aligned}\tag{70}$$

which has the advantage that one can use (68) and (69) at all points of the grid and also numerically guarantees that (66) is satisfied at the poles. It should be remarked that this is not an extra assumption, since it is just a convenient way to incorporate (66) in the code.

For the nonaxially symmetric case, we plan to use other methods in order to circumvent the usual numerical problems at the axis using standard spherical coordinates.

In order to obtain more convenient expressions to compute the right-hand side of Eq. (65), we can start with the coefficient

$$\left(\partial_r\sqrt{\mathcal{R}}+\partial_\theta k+\frac{\cos(\theta)}{\sin(\theta)}k\right), \tag{71}$$

where the last term seems to be problematic at the poles. In this case, we can use l'Hôpital's rule at the poles

$$\lim_{\theta=0,\pi}\frac{\cos(\theta)}{\sin(\theta)}k(r,\theta) = \partial_\theta k(r,\theta)|_{\theta=0,\pi}. \tag{72}$$

The first term of coefficient (71),

$$\partial_r\sqrt{\mathcal{R}} = \frac{4r(r^2+a^2)-\Delta\partial_r K(r,\theta)-K(r,\theta)(2r-2m)}{2\sqrt{\mathcal{R}}}, \tag{73}$$

can also be expressed in a more convenient way in order to avoid r derivatives. We can use the K equation, see [18],

$$\frac{\partial K}{\partial r} = - \pm|_h \frac{\sqrt{\Theta}}{\sqrt{\mathcal{R}}} \frac{\partial K}{\partial \theta}, \tag{74}$$

where $\Theta = K(r,\theta) - a^2 \sin(\theta)^2$. Then we can express (73) as

$$\partial_r \sqrt{\mathcal{R}} = \frac{4r(r^2 + a^2) \pm|_h \Delta \frac{\sqrt{\Theta}}{\sqrt{\mathcal{R}}} \frac{\partial K}{\partial \theta} - K(2r - 2m)}{2\sqrt{\mathcal{R}}}, \tag{75}$$

which can also be expressed in terms of k, by using the relation of Eq. (18) to obtain

$$\begin{aligned}\partial_r \sqrt{\mathcal{R}} = {}& \frac{4r(r^2 + a^2)}{2\sqrt{\mathcal{R}}} \\ &+ \frac{\Delta \frac{k(r,\theta)}{\sqrt{\mathcal{R}}} (2a^2 \sin(\theta) \cos(\theta) + 2k(r,\theta) \partial_\theta k(r,\theta))}{2\sqrt{\mathcal{R}}} \\ &- \frac{(a^2 \sin^2(\theta) + k^2(r,\theta))(2r - 2m)}{2\sqrt{\mathcal{R}}}.\end{aligned} \tag{76}$$

E. Grid construction

In Eq. (65) the coordinate r appears explicitly. However, for each pair of values U, V, there is a two-dimensional surface r_s, which in Boyer-Lindquist coordinates is described by $r(\theta)$, see [18]. Such relation is also revealed in Eq. (33). Therefore, to compute the right-hand side of (65) we need a relation of the type $r = r(U, V, \theta)$. We can start with Eq. (33) and evaluate at $\theta = 0$,

$$UV + \frac{(r - r_+)(r - r_-)^{-\frac{r_-}{r_+}} e^{2\kappa_+ r} (r_-)^{\frac{r_-}{r_+}}}{r_+} = 0. \tag{77}$$

Then, from (77), one can use any numerical method to compute $r(U, V, \theta = 0)$. We have used the Newton-Raphson method with precision error of 1×10^{-14}.

The next step is to compute the full dependence $r(U, V, \theta)$. For a pair of fixed values U_s, V_s, one gets the differential equation for $r(\theta)$ (two-dimensional spacelike surface r_s), see [18],

$$\frac{dr}{d\theta} = -\frac{k(r,\theta)\Delta}{\sqrt{\mathcal{R}}}, \tag{78}$$

where the initial data for Eq. (78) are

$$r(\theta = 0) = r_0(U_s, V_s, \theta = 0). \tag{79}$$

We integrate Eq. (78) with the fourth-order Runge-Kutta method (RK4). Note that, in each RK4 step, a new value like $r(\theta + h_\theta)$ will be out of the original grid where $k(r, \theta)$ was computed. Therefore, we use a bidimensional interpolation method with Legendre polynomials in order to evaluate the right-hand side of Eq. (78), even in every intermediate step of RK4. We have double checked these calculations by also solving (33) by the secant method.

V. NUMERICAL EVOLUTION

A. The grid

We chose to work on the domain

$$U \in [U_0 = -1, U_m = 1], \tag{80}$$

$$V \in [V_0 = 0.5, V_m = 2.5], \tag{81}$$

$$\theta \in [0, \pi]. \tag{82}$$

Numerically, we use a grid of $N_U = N_V = 301$ and $N_\theta = 201$ points, with grid spacing

$$h_U \approx 6.66 \times 10^{-3}, \tag{83}$$

$$h_V \approx 6.66 \times 10^{-3}, \tag{84}$$

$$h_\theta \approx 1.57 \times 10^{-2}. \tag{85}$$

It was verified numerically that such grid spacing satisfies the CFL condition.

B. Sets of initial data

Based on previous works [16,17], the spacetime region $\mathcal{D}$ where we place initial data is

$$\mathcal{D} \coloneqq \{(U_0, V, \theta) \cup (U, V_0, \theta)\}, \tag{86}$$

which graphically consists of two lines in the causal diagram (see Fig. 2), namely, $U = U_0$ and $V = V_0$ (orthogonal lines between each other). In a similar way as [16], the initial data are given by

$$\Phi(U_0, V, \theta) \neq 0, \tag{87}$$

$$\Phi(U, V_0, \theta) = 0. \tag{88}$$

In the conformal diagram of Fig. 2, there is an scaled representation of the initial data domain and the whole numerical evolution domain. Note that, using c.m. double null coordinates, one obtains, for the first time, a conformal causal description of spacetime, with full angular dependence $\theta \in [0, \pi]$ and $\varphi = [0, 2\pi]$. Previous conformal diagrams in literature, see [24,25], were restricted to $\theta = 0, \pi$, which means only along the axis of symmetry. More details about this subject will be published in a separate article.

We decided to work with different types of initial data in order to show the robustness of the numerical scheme and code. The first initial data type has a bell shape on (V, θ). We call it "Bell-init data" and it is defined by

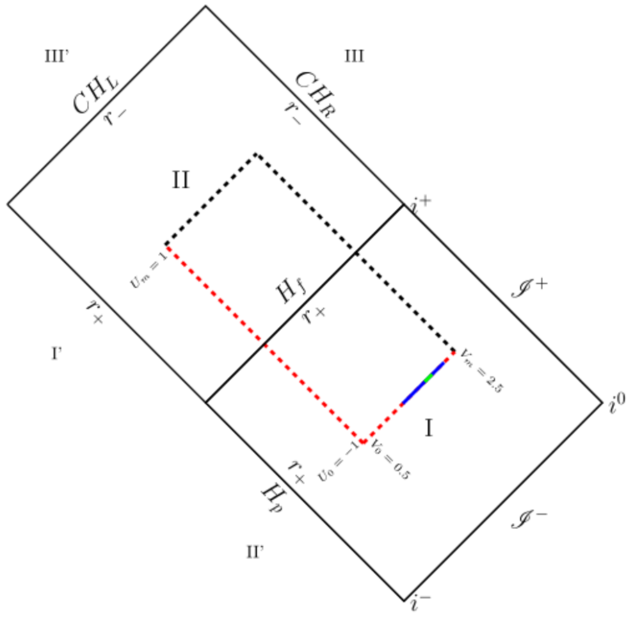

FIG. 2. Conformal diagram of Kerr spacetime in c.m. double null coordinates. The initial data domain is drawn with dashed lines in red color. The initial data $\Phi(U_0 = -1, V, \theta)$ are nonzero over the blue line for armonic-init data (see Fig. 4 for angular dependence on θ) and nonzero over the green line for Bell-init data (see Fig. 3 for angular dependence on θ). The whole domain of numerical evolution is the rectangle delimited by dashed lines (black and red).

$$\Phi(U_0, V, \theta) = \frac{1}{(\sigma_V \sigma_\theta)^8}[V - (V_{\text{center}} - \sigma_V)]^4 \times [V - (V_{\text{center}} + \sigma_V)]^4 \times [\theta - (\theta_{\text{center}} - \sigma_\theta)]^4 \times [\theta - (\theta_{\text{center}} + \sigma_\theta)]^4. \tag{89}$$

In Fig. 3 we have chosen the values $V_{\text{center}} = 1.5$, $\sigma_V = 0.1$, $\theta_{\text{center}} = 0.45\pi$, and $\sigma_\theta = 0.2\pi$. The second initial data type has the same angular dependence of the spherical harmonic $Y_{20}(\theta)$. We call it "Armonic-init data" and it is defined by

$$\Phi(U_0, V, \theta) = A\frac{\sqrt{5}}{4\pi}(3\cos^2(\theta) - 1)[V - (V_{\text{center}} - \sigma_V)]^4 \times [V - (V_{\text{center}} + \sigma_V)]^4. \tag{90}$$

In Fig. 4 we have chosen the values $V_{\text{center}} = 1.5$, $\sigma_V = 0.5$, and $A = 800$.

C. Numerical results

The functional dependence of $\Phi(U, V, \theta)$ and the restriction of three-dimensional plots reduces the information that can be shown in one plot. For this reason, it will be useful to use two complementary plot types.

One of them is $\Phi(U = \text{constant}, V, \theta)$, which shows the wave behavior of the scalar field solution as one increment U; we call it "wave-plot type." The numerical results with wave-plot type for both initial data can be seen in Figs. 5 (for Bell-init data) and 7 (for armonic-init data).

The other complementary plot type is $\Phi(U, V, \theta = \text{constant})$; we call it "causal-plot type." It means that, for each angle $\theta = \text{constant}$, we can see the whole causal evolution over coordinates U, V. The numerical results with causal-plot type can be seen in Figs. 6 (for Bell-init data) and 8 (for armonic-init data).

About the numerical evolution results, one can highlight the smooth behavior across the exterior future horizon H_f ($U = 0 \equiv r = r_+$), as we expected from previous sections (see Supplemental Material [27]).

D. Q precision test

We have already mentioned that the numeric scheme was designed to be second-order accurate. Nevertheless, one can actually verify and test such precision numerically. One can compute a coefficient test Q_{test} that is related with the global precision of the numeric code. For this computation,

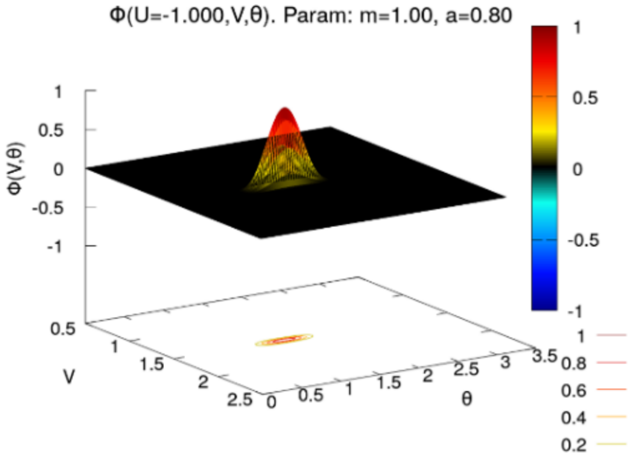

FIG. 3. Plot of Bell-init data, defined by (89), with parameters $V_{\text{center}} = 1.5$, $\sigma_V = 0.1$, and $\theta_{\text{center}} = 0.45\pi$.

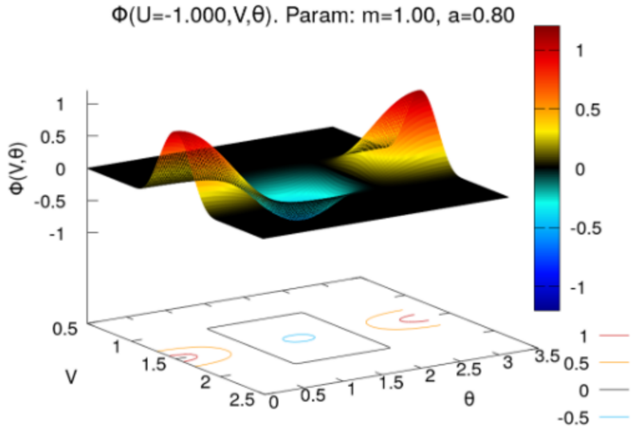

FIG. 4. Plot of armonic-init data, defined by (90), with parameters $V_{\text{center}} = 1.5$, $\sigma_V = 0.5$, and $A = 800$.

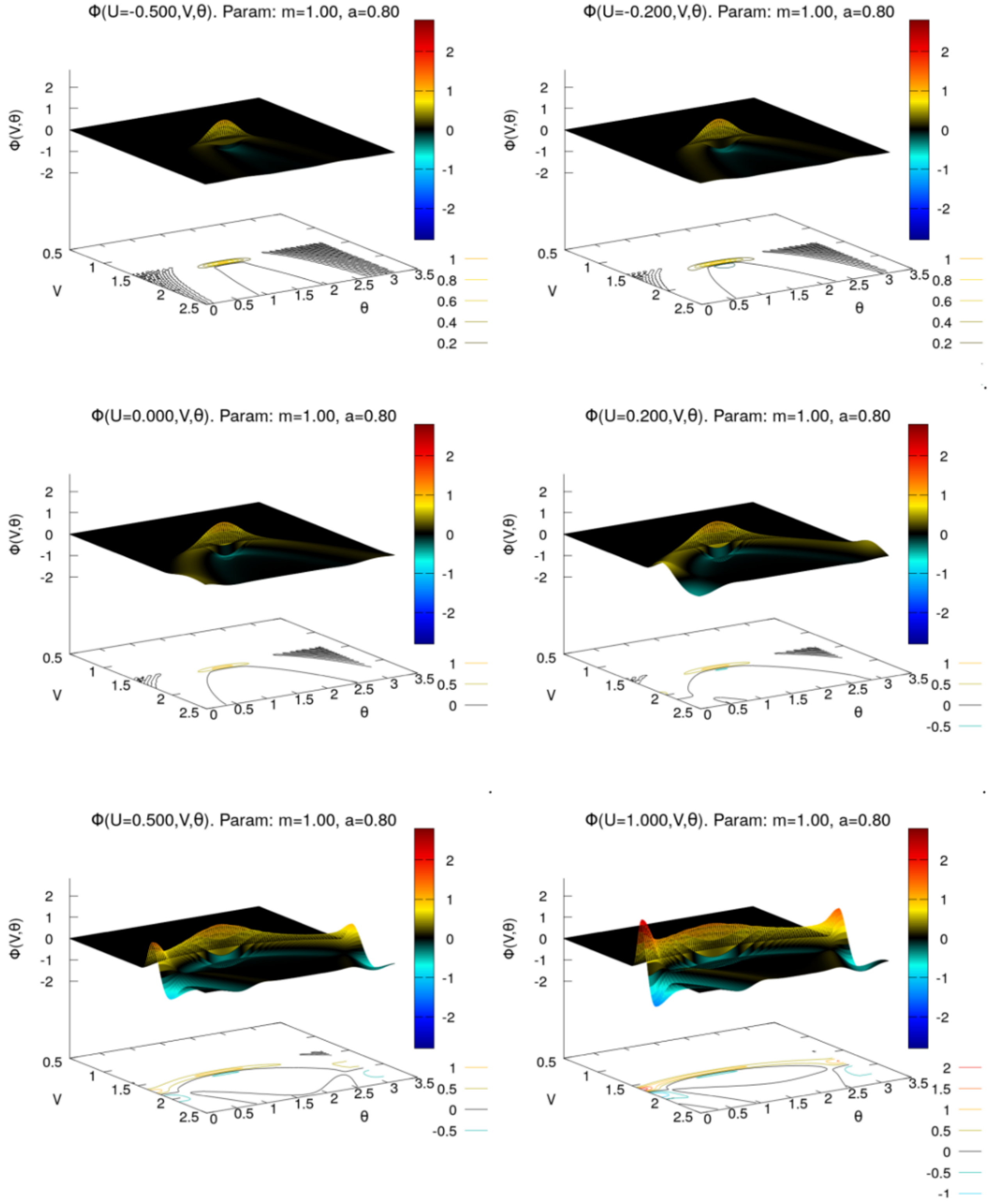

FIG. 5. Numerical evolution of Bell-init data. Each plot shows $\Phi(U = \text{constant}, V, \theta)$ (wave-plot type). The numerical evolution starts with initial data at $U = -1$ (see Fig. 3) and evolves up to $U = 1$. It can be seen that the behavior across the exterior future horizon H_f ($U = 0 \equiv r_+$) is clearly smooth, as we expected based on previous and detailed analysis. One can also see the nontrivial angular dependence with respect to θ. Kerr parameters $a = 0.8$, $m = 1$.

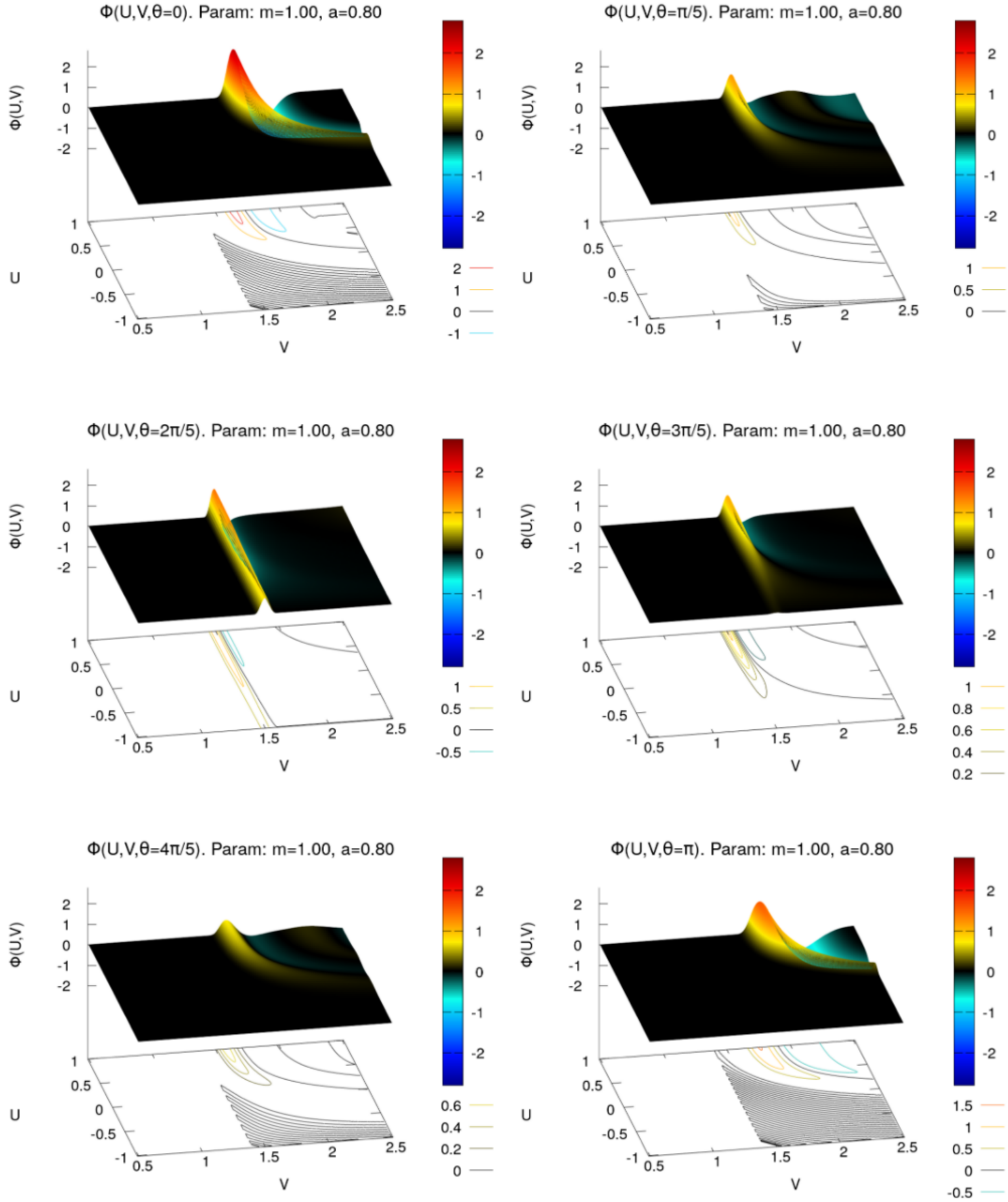
Φ(U,V,θ=0). Param: m=1.00, a=0.80

Φ(U,V,θ=π/5). Param: m=1.00, a=0.80

Φ(U,V,θ=2π/5). Param: m=1.00, a=0.80

Φ(U,V,θ=3π/5). Param: m=1.00, a=0.80

Φ(U,V,θ=4π/5). Param: m=1.00, a=0.80

Φ(U,V,θ=π). Param: m=1.00, a=0.80

FIG. 6. Numerical evolution of Bell-init data. Each plot shows $\Phi(U, V, \theta = \text{constant})$ (causal-plot type). The numerical evolution starts with initial data at $U = -1$ (see Fig. 3) and evolves up to $U = 1$. It can be seen that the behavior across the exterior future horizon H_f $(U = 0 \equiv r_+)$ is clearly smooth, as we expected based on previous and detailed analysis. In this case, one gets the whole causal picture in terms of U, V coordinates, but at fixed values of θ. Kerr parameters $a = 0.8$, $m = 1$.

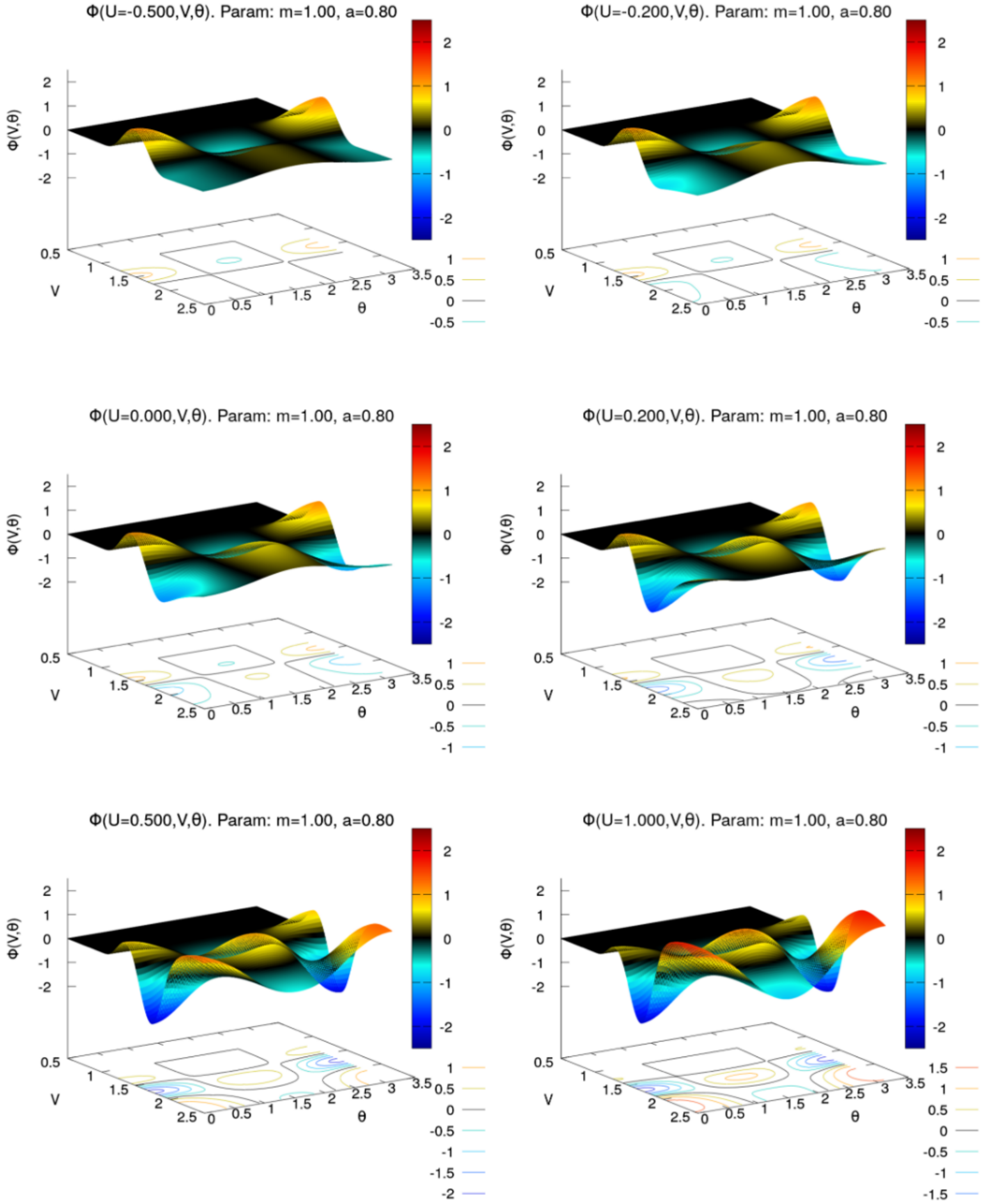

FIG. 7. Numerical evolution of armonic-init data. Each plot shows $\Phi(U = \text{constant}, V, \theta)$ (wave-plot type). The numerical evolution starts with initial data at $U = -1$ (see Fig. 3) and evolves up to $U = 1$. It can be seen that the behavior across the exterior future horizon H_f $(U = 0 \equiv r_+)$ is clearly smooth, as we expected based on previous and detailed analysis. One can also see the nontrivial angular dependence with respect to θ. Kerr parameters $a = 0.8$, $m = 1$.

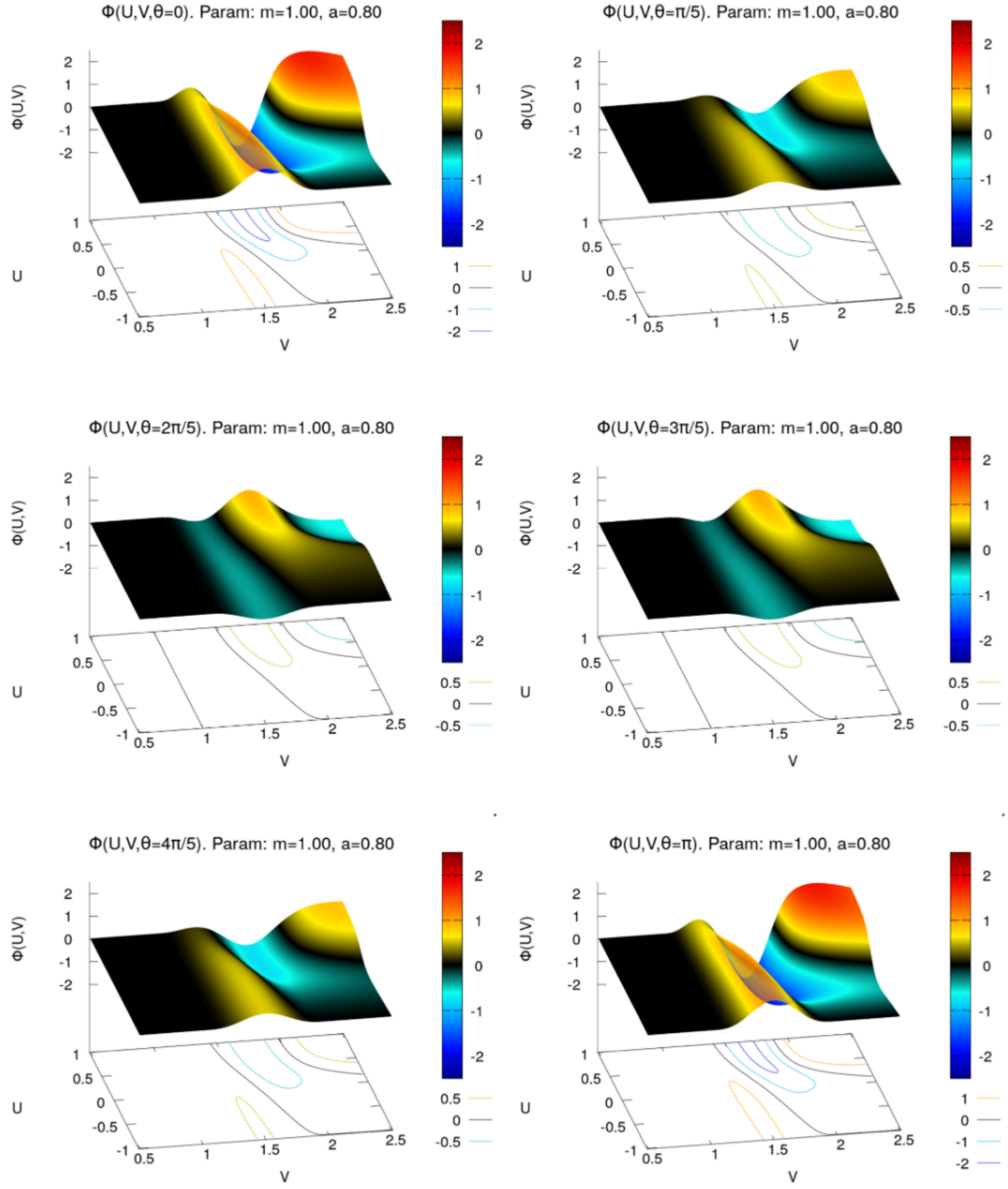

FIG. 8. Numerical evolution of armonic-init data. Each plot shows $\Phi(U, V, \theta = \text{constant})$ (causal-plot type). The numerical evolution starts with initial data at $U = -1$ (see Fig. 3) and evolves up to $U = 1$. It can be seen that the behavior across the exterior future horizon H_f $(U = 0 \equiv r_+)$ is clearly smooth, as we expected based on previous and detailed analysis. In this case, one gets the whole causal picture in terms of U, V coordinates, but at fixed values of θ. Kerr parameters $a = 0.8$, $m = 1$.

one needs the numerical solutions with grid spacing $h, \frac{h}{2}$ and $\frac{h}{4}$, where $h = h_U = h_V$. Then,

$$Q_{\text{test}}(U,V) = \frac{\int_0^\pi [\Phi(h,h_\theta) - \Phi(\frac{h}{2},h_\theta)]^2 d\theta}{\int_0^\pi [\Phi(\frac{h}{2},h_\theta) - \Phi(\frac{h}{4},h_\theta)]^2 d\theta} \approx 2^p, \quad (91)$$

where p is the precision order of the code; it means that the global error is $\mathcal{O}(h)^p$.

We have computed Q_{test} in the whole domain U, V, for the numerical evolution of each initial data. In all cases, it was obtained that $Q_{\text{test}} \approx 4$, which means that the numerical scheme and the implemented numeric code is second-order accurate with global error $\mathcal{O}(h^2)$. This result was expected by numerical scheme design (45). The numeric computation of Q_{test} is shown in Figs. 9 (for Bell-init data) and 10 (for armonic-init data).

E. Energy conservation test

The massless scalar field equation can also be written as

$$\nabla^a \nabla_a \Phi = 0, \quad (92)$$

where its related energy-momentum tensor is

$$T_{ab} = \nabla_a \Phi \nabla_b \Phi - \frac{1}{2} g_{ab} \nabla_c \Phi \nabla^c \Phi. \quad (93)$$

From (92) and (93) it is straightforward to show that

$$\nabla_a T^a{}_b = 0, \quad (94)$$

which allows one to define a conserved quantity. If one uses a Killing vector ξ, the next result follows:

$$\nabla_a (T^a{}_b \xi^b) = (\nabla_a T^a{}_b) \xi^b + T^a{}_b \nabla_a \xi^b = 0, \quad (95)$$

where the first term of Eq. (95) is zero because of Eq. (94) and the second term is zero because of the symmetry $(T_{ab} = T_{ba})$ together with the Killing vector property $(\nabla_a \xi^b + \nabla_b \xi^a = 0)$. As usual, one can define a related current for this conservation law,

$$J^a = T^a{}_b \xi^b. \quad (96)$$

The application of Stokes' theorem to this case, for a region $\mathcal{V}$ bounded by the future hypersurface $S_f = U_f \cup V_f$ and the past hypersurface $S_p = U_p \cup V_p$, can be expressed as

$$\begin{aligned} \int_{\mathcal{V}} \nabla_a J^a d\mathcal{V} &= \int_{\mathcal{V}} \frac{1}{\sqrt{g}} \frac{\partial}{\partial x^\mu} (\sqrt{g} J^\mu)(\sqrt{g} dU dV d\theta d\varphi) \\ &= \int_{V_p}^{V_f} (J^U \sqrt{g})_{|_{U_f}} dV d\theta d\varphi \\ &\quad + \int_{U_p}^{U_f} (J^V \sqrt{g})_{|_{V_f}} dU d\theta d\varphi \\ &\quad - \int_{V_p}^{V_f} (J^U \sqrt{g})_{|_{U_p}} dV d\theta d\varphi \\ &\quad - \int_{U_p}^{U_f} (J^V \sqrt{g})_{|_{V_p}} dU d\theta d\varphi = 0. \end{aligned} \quad (97)$$

Then one can define a future and past energy

$$\begin{aligned} E_f &= \int_{V_p}^{V_f} (J^U \sqrt{g})_{|_{U_f}} dV d\theta d\varphi \\ &\quad + \int_{U_p}^{U_f} (J^V \sqrt{g})_{|_{V_f}} dU d\theta d\varphi, \end{aligned} \quad (98)$$

$$\begin{aligned} E_p &= \int_{V_p}^{V_f} (J^U \sqrt{g})_{|_{U_p}} dV d\theta d\varphi \\ &\quad + \int_{U_p}^{U_f} (J^V \sqrt{g})_{|_{V_p}} dU d\theta d\varphi. \end{aligned} \quad (99)$$

Note that, from (97), both quantities must be conserved, which means they must have the same value.

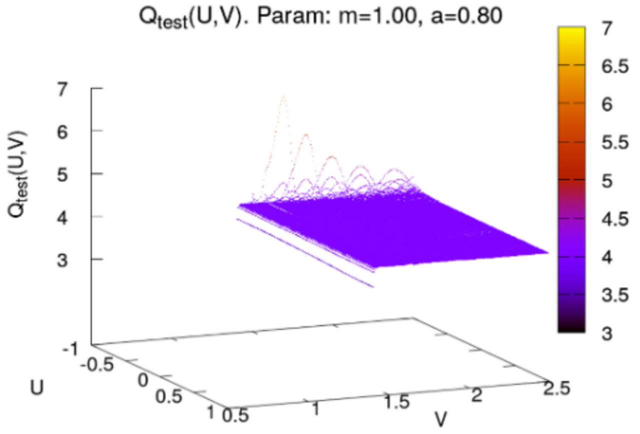

FIG. 9. Plot of precision test $Q_{\text{test}}(U,V)$ for Bell-init data.

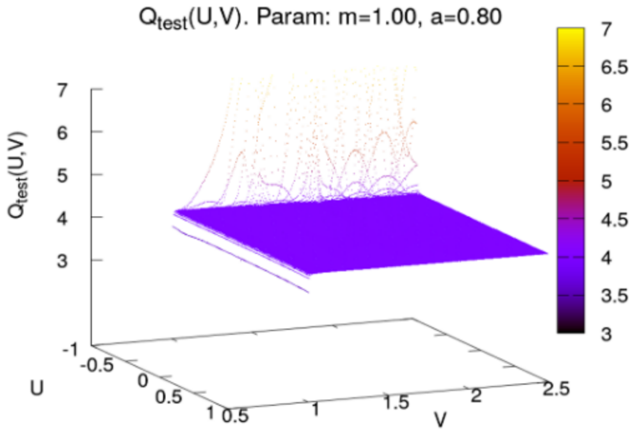

FIG. 10. Plot of precision test $Q_{\text{test}}(U,V)$ for armonic-init data.

In this work we will use the Killing vector

$$\xi^b = \left(\frac{\partial}{\partial t}\right)^b = \left(-\kappa_+ U \frac{\partial}{\partial U} + \kappa_+ V \frac{\partial}{\partial V}\right)^b, \qquad (100)$$

which allows one to obtain explicit expressions for J^U and J^V, namely,

$$\begin{aligned} J^U &= T^a{}_b \xi^b (dU)_a = T^U{}_b \xi^b \\ &= \kappa_+ \bigg[V g^{\mathrm{UV}} \left(\frac{\partial}{\partial V}\Phi\right)^2 \\ &\quad + (V g^{U\theta} + U g^{V\theta}) \left(\frac{\partial}{\partial V}\Phi\right)\left(\frac{\partial}{\partial \theta}\Phi\right) \\ &\quad + \frac{1}{2} U g^{\theta\theta} \left(\frac{\partial}{\partial \theta}\Phi\right)^2 \bigg], \end{aligned} \qquad (101)$$

$$\begin{aligned} J^V &= T^a{}_b \xi^b (dV)_a = T^V{}_b \xi^b \\ &= -\kappa_+ \bigg[U g^{\mathrm{UV}} \left(\frac{\partial}{\partial U}\Phi\right)^2 \\ &\quad + (V g^{U\theta} + U g^{V\theta}) \left(\frac{\partial}{\partial U}\Phi\right)\left(\frac{\partial}{\partial \theta}\Phi\right) \\ &\quad + \frac{1}{2} V g^{\theta\theta} \left(\frac{\partial}{\partial \theta}\Phi\right)^2 \bigg]. \end{aligned} \qquad (102)$$

In the numerical evolution, the limits of V domain has fixed values, where $V_p = V_0 = 0.5$ and $V_f = V_m = 2.5$ [see Eq. (80)]. Then, during the numerical evolution, for each step in U, we can compute E_p and E_f, which is naturally adapted to the double null numerical scheme. Therefore, the relative variation of the conserved energy can be computed numerically as

$$\mathcal{E}_{\mathrm{relative}} = \frac{E_f(U) - E_p(U)}{E_p(U)}, \qquad (103)$$

where each one of $E_p(U)$ and $E_f(U)$ are integrated over different hypersurfaces. In the conformal spacetime diagram, those different hypersurfaces look like different pair sides in the rectangle domain. For example, in Fig. 11 it is shown the regions where $E_p(U)$ (red lines) and $E_f(U)$ (violet lines) are computed, for two cases: $U = -0.5$ and $U = 0.5$.

The main importance of the conserved energy is to provide a totally independent way to measure the quality of the numeric evolution, in the sense that it is very sensible to any departure from the original scalar field equation. The results of energy conservation for each initial data type are shown in Figs. 12 and 13. In one case the variation was less than 0.003% and in the other the energy variation is less than 0.005%. This means that the scalar field behavior revealed in our numerical solutions is highly reliable and accurate.

It is worthwhile to note that h_U and h_V do not have units. Then, the natural question might be "is our grid small or big?"

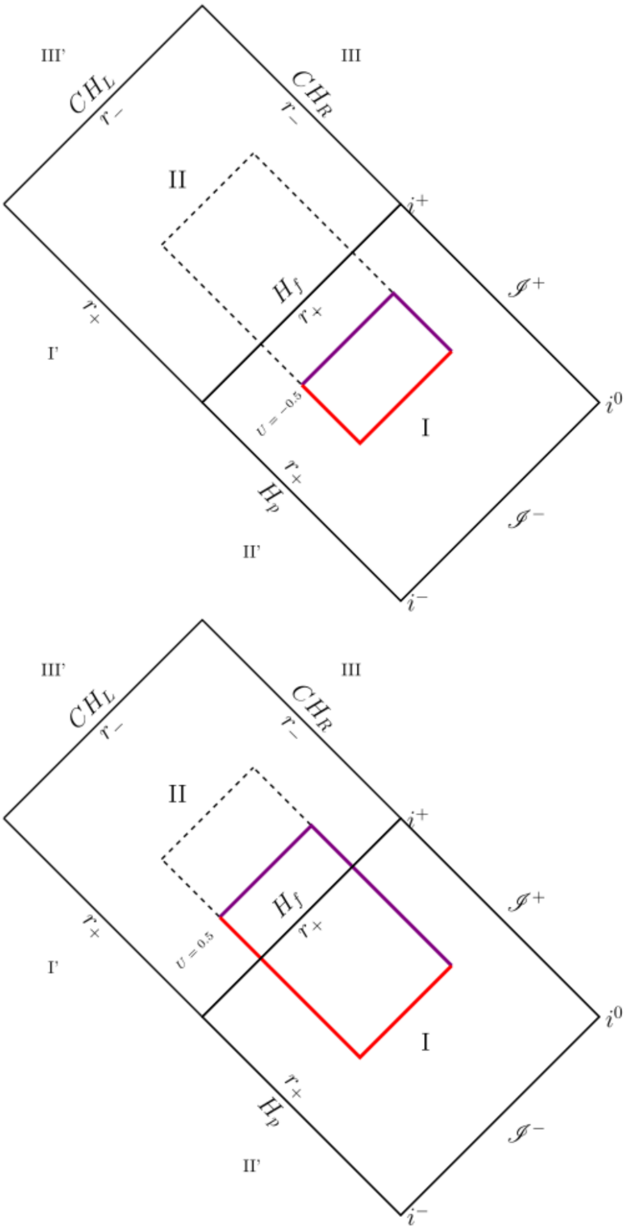

FIG. 11. Conformal diagram of Kerr spacetime in c.m. double null coordinates. Red lines show the region where past energy $E_p(U)$ is computed, and violet lines shows where future energy $E_f(U)$ is computed. Two cases are shown: $U = -0.5$ and $U = 0.5$.

Or, in other words, is it a low or high resolution grid? To clarify this, we observe here the relation between these two coordinates close to the horizon. Let us see that in the chosen grid the starting point $U = -1$ corresponds to $u = 0$, but after 148 steps, one has $U_{148} = -0.01333$ which corresponds to $u_{148} = 23.026$, which has the same units as m. Then, the next step is 149, which brings us to $U_{149} = -0.0066$ and $u_{149} = 26.723$; whereas the horizon is reached at the 150th step with $U_{150} = 0.0$ and $u_{150} = \infty$. If we were to take a new grid with half the value of h_U, we would be dealing with 600 intervals, and the exercise above would now

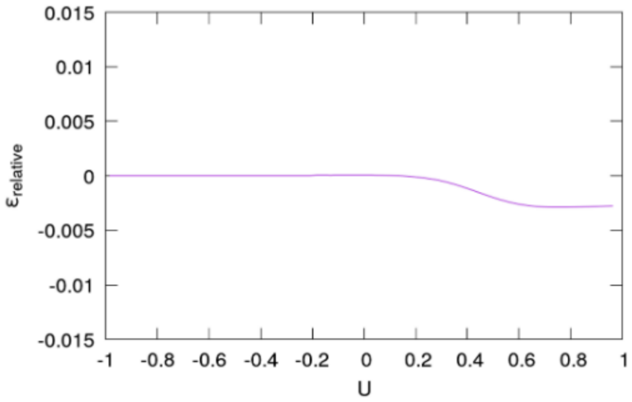

FIG. 12. Relative energy variation given by Eq. (103) for numerical evolution of Bell-init data. Note that the variation is less than 0.003%.

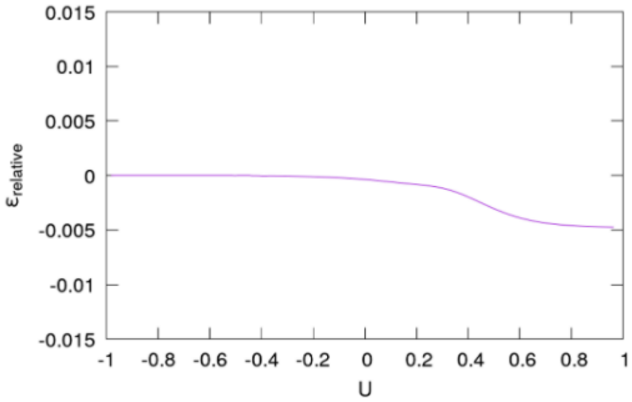

FIG. 13. Relative energy variation given by Eq. (103) for numerical evolution of armonic-init data. Note that the variation is less than 0.005%.

be concerned with the corresponding values near the horizon given by $u_{298} = 26.723$, $u_{299} = 30.420$, and $u_{300} = \infty$. So, one can see that, due to the logarithmic relation between u and U, even when one decreases the interval h_U linearly, one still finds big intervals in u and the final inevitable infinite interval just before reaching the horizon. This tells us that the convenient geometrical coordinate U, which allows us to cross the horizon smoothly, always generates a coarse, low resolution grid, close to the horizon in the asymptotic region, where an increment in u can be associated with asymptotic retarded time. For this reason, one has to choose very carefully the appropriate null coordinates, depending on the objectives of the calculation.

As far as we know, there is no precedent in literature of this type of calculation in double null coordinates for Kerr spacetime.

Our understanding of the small variations in Figs. 12 and 13 is that they reflect the limitation of using a second-order evolution scheme. In further works, this can be improved by the use of other numerical methods to manage the angular derivatives with more sophisticated techniques. Nevertheless, the results of this work clearly show the feasibility of solving the scalar field equation in double null coordinates.

VI. FINAL COMMENTS

This is the first time that a double null coordinate system was used to solve the scalar field equation in Kerr spacetime. The results provide a clear example of how useful the c.m. double null coordinate system can be, which is well behaved throughout the spacetime including the axis of symmetry, unlike previous attempts in the literature [19–22]. The numerical scheme and code development clearly establish the feasibility of solving these types of equations with nontrivial angular dependence at second-order precision in grid spacing, that is, with a global error of the order $\mathcal{O}[h^2]$. Such precision follows from design; nevertheless, it was also tested numerically, obtaining full consistent results.

Among the advantages of null-null decomposition $(2+2)$, we find that they allow a direct causal interpretation, which is more useful when evolving toward the horizon H_f and interior regions. On the other hand, it reduces the complexity of differential equations. In the spatial-temporal decomposition $(3+1)$, one has to deal with second-order derivatives in time and space; meanwhile in null-null decomposition $(2+2)$, one only has first derivatives with respect to each null coordinate.

In this work we have shown that the scalar field equation is well behaved across future and past exterior event horizons H_f and H_p, from a fundamental analytical point of view. We have also shown that numerical solutions are well behaved across the future exterior horizon H_f, as we expected.

The numerical result's fidelity was tested with an independent procedure of energy conservation. The energy variation was less than 0.003% in one case and less than 0.005% in the other, which manifest the reliability and accuracy of the numerical evolution.

The study of the solutions of the scalar field equation allows us to tackle the principal part of the Teukolsky equation [1], which can be used to describe possible linear perturbations of Kerr spacetime. Therefore, this work can be extended to the study of linear perturbations of spin weight 1 (electromagnetic field) and 2 (gravitational waves), opening a new avenue for Kerr stability studies in double null coordinates. We plan to work on these kinds of linear perturbations in future works.

ACKNOWLEDGMENTS

We have benefited from comments from Miguel Megevand and Manuel Tiglio, and we are also grateful to Luis Lehner for questions and suggestions. We also would like to thank the comments and criticism from an anonymous Referee that led us to a further improvement of the manuscript. We acknowledge support from CONICET, SeCyT-UNC, and FONCYT.

[1] Saul A. Teukolsky, Rotating Black Holes: Separable Wave Equations for Gravitational and Electromagnetic Perturbations, Phys. Rev. Lett. **29**, 1114 (1972).

[2] B. P. Abbott *et al.* (The LIGO Scientific Collaboration), Observation of Gravitational Waves from a Binary Black Hole Merger, Phys. Rev. Lett. **116**, 061102 (2016).

[3] EHT Collaboration, First M87 Event Horizon Telescope results. IV. Imaging the central supermassive black hole, Astrophys. J. Lett. **875**, L4 (2019).

[4] Izak Thuestad, Gaurav Khanna, and Richard H. Price, Scalar fields in black hole spacetimes, Phys. Rev. D **96**, 024020 (2017).

[5] Lior M. Burko, Gaurav Khanna, and Anıl Zenginoğlu, Cauchy-horizon singularity inside perturbed Kerr black holes, Phys. Rev. D **93**, 041501 (2016).

[6] Donald Marolf and Amos Ori, Outgoing gravitational shock wave at the inner horizon: The late-time limit of black hole interiors, Phys. Rev. D **86**, 124026 (2012).

[7] István Rácz and Gábor Zs Tóth, Numerical investigation of the late-time Kerr tails, Classical Quantum Gravity **28**, 195003 (2011).

[8] Manuela Campanelli, Gaurav Khanna, Pablo Laguna, Jorge Pullin, and Michael P. Ryan, Perturbations of the Kerr spacetime in horizon-penetrating coordinates, Classical Quantum Gravity **18**, 1543 (2001).

[9] Amos Ori, Oscillatory Null Singularity inside Realistic Spinning Black Holes, Phys. Rev. Lett. **83**, 5423 (1999).

[10] Amos Ori, Structure of the Singularity inside a Realistic Rotating Black Hole, Phys. Rev. Lett. **68**, 2117 (1992).

[11] R. K. Sachs, Gravitational waves in general relativity VIII: Waves in asymptotically flat space-time, Proc. R. Soc. A **270**, 103 (1962).

[12] R. Penrose, Zero rest-mass fields including gravitation: Asymptotic behaviour, Proc. R. Soc. A **284**, 159 (1965).

[13] Manuel Tiglio, Lawrence E. Kidder, and Saul A. Teukolsky, High accuracy simulations of Kerr tails: Coordinate dependence and higher multipoles, Classical Quantum Gravity **25**, 105022 (2008).

[14] A. D. Rendall, Reduction of the characteristic initial value problem to the Cauchy problem and its applications to the Einstein equations, Proc. R. Soc. A **427**, 221 (1990).

[15] Jonathan Luk and Jan Sbierski, Instability results for the wave equation in the interior of Kerr black holes, J. Funct. Anal. **271**, 1948 (2016).

[16] Carsten Gundlach, Richard H. Price, and Jorge Pullin, Late time behavior of stellar collapse and explosions: 1. Linearized perturbations, Phys. Rev. D **49**, 883 (1994).

[17] Ehud Eilon and Amos Ori, Adaptive gauge method for long-time double null simulations of spherical black-hole spacetimes, Phys. Rev. D **93**, 024016 (2016).

[18] Marcos A. Argañaraz and Osvaldo M. Moreschi, Double null coordinates for Kerr spacetime, Phys. Rev. D **104**, 024049 (2021).

[19] Sean A. Hayward, Kerr Black Holes in Horizon-Generating Form, Phys. Rev. Lett. **92**, 191101 (2004).

[20] S. J. Fletcher and A. W. C. Lun, The Kerr spacetime in generalized Bondi-Sachs coordinates, Classical Quantum Gravity **20**, 4153 (2003).

[21] Nigel T. Bishop and Liebrecht R. Venter, Kerr metric in Bondi-Sachs form, Phys. Rev. D **73**, 084023 (2006).

[22] Frans Pretorius and Werner Israel, Quasispherical light cones of the Kerr geometry, Classical Quantum Gravity **15**, 2289 (1998).

[23] Robert H. Boyer and Richard W. Lindquist, Maximal analytic extension of the Kerr metric, J. Math. Phys. (N.Y.) **8**, 265 (1967).

[24] Brandon Carter, Global structure of the Kerr family of gravitational fields, Phys. Rev. **174**, 1559 (1968).

[25] Subrahmanyan Chandrasekhar, *The Mathematical Theory of Black Holes* (Oxford University Press, 1983), 10.1007/978-94-009-6469-3_2.

[26] Roberto Gomez, Willians Barreto, and Simonetta Frittelli, A framework for large-scale relativistic simulations in the characteristic approach, Phys. Rev. D **76**, 124029 (2007).

[27] See Supplemental Material at http://link.aps.org/supplemental/10.1103/PhysRevD.105.084012 for videos of numerical evolution with initial data at $U = -1$ evolving up to $U = 1$. The behavior across the exterior future horizon ($U = 0$) is clearly smooth.

Universidad Nacional de Córdoba
1983/2023 - 40 AÑOS DE DEMOCRACIA

Hoja Adicional de Firmas
Informe Gráfico

Número: IF-2023-00750796-UNC-ME#FAMAF

CORDOBA, CORDOBA
Viernes 1 de Septiembre de 2023

Referencia: MORESCHI- Documentacion informe año sabatico parte 1//
EX-2021-00478970- -UNC-ME#FAMAF

El documento fue importado por el sistema GEDO con un total de 17 pagina/s.

Digitally signed by GDE UNC
DN: cn=GDE UNC, c=AR, o=Universidad Nacional de Cordoba, ou=Informatica, serialNumber=CUIT 30546670623
Date: 2023.09.01 12:23:41 -03'00'

SILVIA ANAHI VERON
Administrativa
Mesa de Entradas Facultad de Matemática, Astronomía, Física y Computación
Universidad Nacional de Córdoba

Digitally signed by GDE UNC
DN: cn=GDE UNC, c=AR, o=Universidad Nacional de Cordoba, ou=Informatica, serialNumber=CUIT 30546670623
Date: 2023.09.01 12:23:50 -03'00'